Tomographic imaging using multi-simultaneous measurements (TIMes) for single-shot emission reconstructions in turbulent spray flames

Fabio J. W. A. Martins[1,*], Cheau Tyan Foo[1], Andreas Unterberger[1], Khadijeh Mohri[1,2,3]

1: Institute for Combustion and Gas Dynamics – Tomography Group, University of Duisburg-Essen, Germany
2: Institute for Combustion and Gas Dynamics – Fluid Dynamics, University of Duisburg-Essen, Germany
3: Center for Nanointegration Duisburg-Essen (CENIDE), Germany
*Corresponding author: fabio.martins@uni-due.de

Keywords: Combustion diagnostics, Multi-spectral measurements, Computed Tomography of Chemiluminescence, CTC

ABSTRACT

Tomographic imaging using multi-simultaneous measurements of emissions is applied to three operating conditions of the SpraySyn burner in order to investigate the turbulent flame morphology and its potential impact on the flame spray pyrolysis. Instantaneous and time-averaged three-dimensional fields of CH* chemiluminescence (flame front marker) and atomic Na emission from NaCl dissolved in the injected liquid solution (linked to hot products of the spray flame) are reconstructed using 29 cameras divided between them. The association between CH* and Na signals is analyzed using isosurface visualizations, combined slices, profiles and scattered p lots. The instantaneous results unveil the complex reacting turbulent flow and regions of interplay between the flame front and the hot spray products. The time-averaged results show that the investigated spray flames are slightly asymmetric near the burner exit and evolve towards symmetric bell-shaped distributions further downstream. In the context of flame spray pyrolysis, the flame asymmetries potentially lead to inhomogeneous characteristics of the final synthesized material.

1. Introduction

Turbulent spray flames are present in many practical applications, such as combustors and flame spray pyrolysis (FSP) (Schulz et al., 2019; Meierhofer & Fritsching, 2021). These flows are complex, since the atomization process and chemical reactions interact under an unsteady three-dimensional (3D) environment exhibiting multiple scales. The atomized droplets are distributed over a range of sizes and their evaporation rate depends on the droplet concentration in the spray and on the local turbulent flow. The evaporating droplets constantly feed the carrier gas with fresh fuel, locally changing the flame stoichiometry. These and other mechanisms, as well as the underlying flow, need to be understood for a good performance of such turbulent spray flame processes.

Tomographic imaging using multi-simultaneous measurements (TIMes) (Foo et al., 2021) is a powerful non-intrusive diagnostic technique that allows the reconstruction of 3D instantaneous fields

of various concurrent signals. Such measurements can aid better understanding turbulent (spray) flames by providing insights into the flame morphology and the interaction between the fields. The viewing sensors in the tomographic arrangement are adjusted to selectively detect various modalities, such as transmission, absorption, scattering or emission signals, which could include the naturally occurring chemiluminescence of the flame as well as emission from tracer species that are seeded into specific streams.

The TIMes technique is employed here to study turbulent spray flames issued through the SpraySyn burner (Schneider et al., 2019). The SpraySyn burner is a standardized lab-scaled reactor that has been introduced in the German DFG-funded Priority Program (SPP1980) to investigate the FSP mechanisms for nanoparticle formation. Flame spray pyrolysis allows the synthesis of a wide range of functional nanoparticles once the process is understood and controlled (Schulz et al., 2019; Meierhofer & Fritsching, 2021). The burner has a simplified geometry and standard operating conditions for systematic comparisons of experiments and simulations among different research groups. The burner is composed of a central twin-fluid nozzle that atomizes a liquid precursor solution by a high-momentum annular dispersion flow of oxygen. The precursor solution is designed according to the desired nanoparticle product at the output. The atomized precursor solution forms a turbulent spray flame that is stabilized by a laminar pilot flame from a premixed methane-oxygen gas flowing in the annular region through a porous matrix. A co-flowing stream of nitrogen, issuing through the same porous matrix at the outermost annulus with a 70-mm outer diameter, shields the main flow against environmental fluctuations and assists in the transport of the synthesized nanoparticles.

In the present work, we apply TIMes by measuring the CH* chemiluminescence and Na emission from the NaCl dissolved in the atomized liquid solution of the SpraySyn burner. The CH* signal is related to the flame front, while the Na signal is linked to the hot spray-flame products, since it only emits at higher temperatures (Mosburger et al., 2014). Studying the interaction between the flame front and spray-flame products is especially important in the context of FPS for nanoparticle synthesis as the final material is directly linked to the temperature-composition history experienced by the nanoparticle (Schulz et al., 2019; Stodt et al., 2021; Tischendorf et al., 2021; Bieber et al., 2021; Meierhofer & Fritsching, 2021).

2. Method

TIMes was applied to various spray flames emanating from the SpraySyn burner for reconstructing the CH* and Na signals. The operating conditions investigated were determined by varying the dispersion gas flow rate (between 9 to $12\,\text{slm}$ of O_2), while maintaining constant flow rates for the premixed pilot flame ($2\,\text{slm}$ of CH_4 and $16\,\text{slm}$ of O_2), the co-flow ($120\,\text{slm}$ of N_2), and the liquid injection ($2\,\text{mL/min}$ of precursor solution). The variation of the flow rates of liquid injection was studied in another work (Foo et al., 2022). The burner here was operated without any enclosure at atmospheric pressure and ambient temperature of $22\,^{\circ}\text{C}$. The liquid injection solution employed in

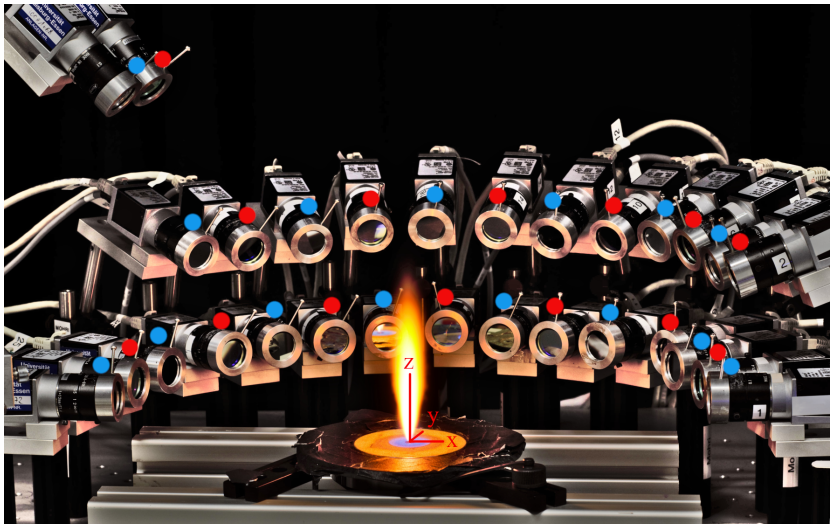

Figure 1. TIMes setup around the SpraySyn burner for simultaneous imaging of the instantaneous 3D fields of CH* (cameras with blue dots) and Na (red dots). The world coordinate system is presented in red.

the present work was composed of trace amount of NaCl dissolved in ethanol with $2.5\,\%\,\mathrm{v/v}$ water content (concentration of $0.0375\,\mathrm{g/L}$). The investigated conditions include the standard operating condition SF1 proposed in Schneider et al. (2019) (i.e., $10\,\mathrm{slm}$ of dispersion gas). The burner and nozzle were carefully aligned before the experiments (Foo et al., 2022).

The measurements were conducted using a generic cost-effective multi-camera setup, consisting of 29 CCD cameras (Basler acA-645-100gm, sensor of 659×494 pixels) as shown in Fig. 1. The cameras used in the setup were split into two categories, with 15 dedicated to detecting CH* chemiluminescence and 14 dedicated to Na emission. These number of cameras are sufficient for accurate measurements (Mohri et al., 2017; Foo et al., 2022). Not requiring external light sources leads to a relatively low-cost and simple experimental setup. The cameras were arranged equiangularly in a $168°$ arc around the burner. They were positioned $320\,\mathrm{mm}$ away from the burner center in three levels. The cameras were equipped with $12\text{-}\mathrm{mm}$ focal-length lenses (Kowa LM12JC) with apertures of $f/1.4$. In order to optically separate the two measured signals, spectral bandpass filters were placed in front of the cameras. The CH* signal was detected through $433-24\,\mathrm{nm}$ BrightLine filters (blue dots in Fig. 1) and the Na signal was detected through $589-10\,\mathrm{nm}$ TECHSPEC filters (red dots). The camera exposure times were adjusted to $450\,\mu\mathrm{s}$ for CH* and to $100\,\mu\mathrm{s}$ for Na due to differences in signal intensities. The values are a compromise between signal-to-noise ratio and motion blur (Mohri et al., 2017). The camera acquisition was synchronously triggered by a pulse generator.

The present turbulent spray flames are unstable and fluctuate over sequences of ignition, combustion, and extinction, as explained by Bieber et al. (2021). The occurrence of extinguished spray flames (leading to acquired images with the lowest intensities) were quantified as $50\,\%$ of the time (Bieber et al., 2021). This probably produces particles following liquid-to-particle conversion, which is generally undesirable in most of FSP processes (Schulz et al., 2019; Meierhofer &

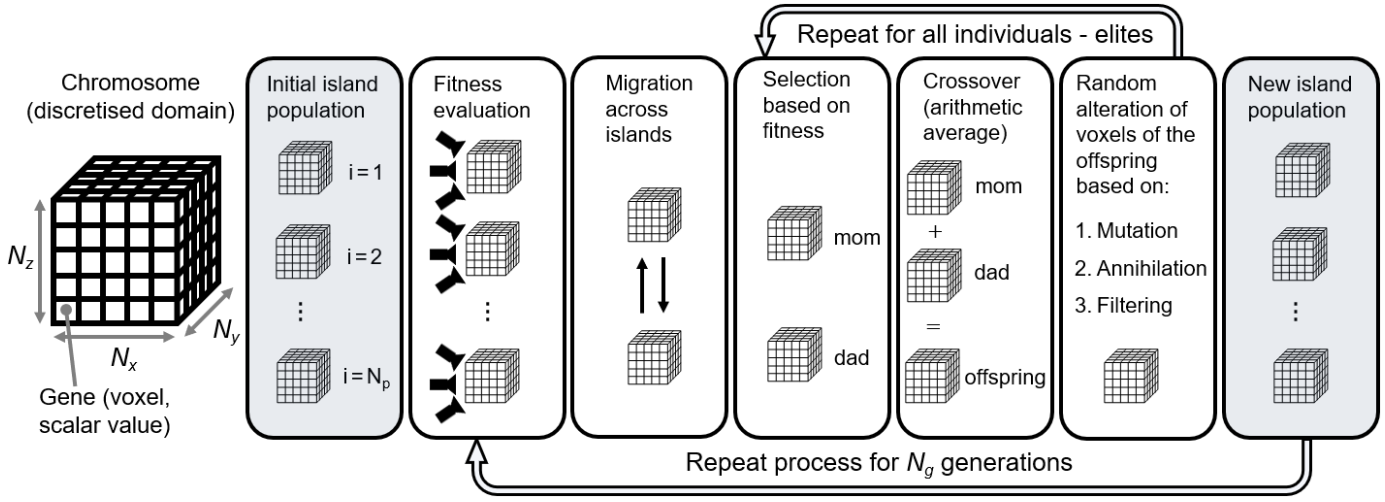

Figure 2. Definition of the chromosome as a discretised reconstruction domain for the CH* and Na fields with each gene representing an intensity value. The evolution step for an island population of N_p chromosomes is repeated for N_g generations and the best individuals are selected based on the fitness evaluation.

Fritsching, 2021). Therefore, from a total of 400 acquired images for each camera at each operating condition, only the 200 brightest images were used for further processing based on the aforementioned time of extinguished spray flames. The images were background subtracted, cropped to a size of 195×302 pixels and resized by a factor of 0.75.

Instantaneous and time-averaged 3D fields of CH* and Na were estimated by feeding the preprocessed images into the Evolutionary Reconstruction Technique (ERT) proposed by Unterberger et al. (2019a). The original ERT for emission reconstructions was further improved by incorporating methodological advances from the evolutionary background oriented Schlieren tomography described by Unterberger & Mohri (2022). The improved ERT technique is based on genetic algorithms in which a population composed of individuals (chromosomes), representing solution candidates for the reconstructed scalar field, evolves over various iterations (generations) by crossover (arithmetic average), mutation, annihilation, and filtering operators. A stochastic mask based on the Metropolis sampling algorithm defines the spatial application of the genetic operators. The population is distributed over islands and the individuals are allowed to migrate. The solution that is selected by the ERT after a sufficient number of generations is the best individual that minimizes the distance between its ray-traced projections and the measurement images. The camera calibration, which is a prerequisite for tomographic imaging, was also performed by means of genetic algorithms assuming a pinhole model and by imaging a phosphorescent 3D target (Unterberger et al., 2019b). The present in-house code runs on parallel GPUs to reduce the computational time. The reconstructed fields of this work are composed of $80 \times 80 \times 160$ voxels (x, y and z-axis, respectively) with a voxel size of $0.375\,\mathrm{mm}$. Each field evolves over $200\,000$ generations from a population of 48 individuals distributed across 4 islands.

3. Results

Typical instantaneous reconstructed fields of CH* and Na signal are presented in Fig. 3 as well as time-averaged fields obtained from 200 measurements. In the figure, blue and cyan isosurfaces correspond to the flame front, while red and yellow isosurfaces to the hot spray-flame products. The fields are normalized by their maximum intensity and shown with a quarter of the domain cut out for better visualization of their inner regions. The structures shown are related to the turbulent spray flames, except for the horizontal annular structures close to the burner surface (C-shaped isosurfaces due to the visualization cut), which are linked to the premixed pilot flame used in the SpraySyn burner for stabilization of the former flames. Minor variations of the pilot flames for each case are observed, as expected due to their laminar nature. The instantaneous flame front structures are more constricted close to the z-axis, in contrast to the instantaneous structures of

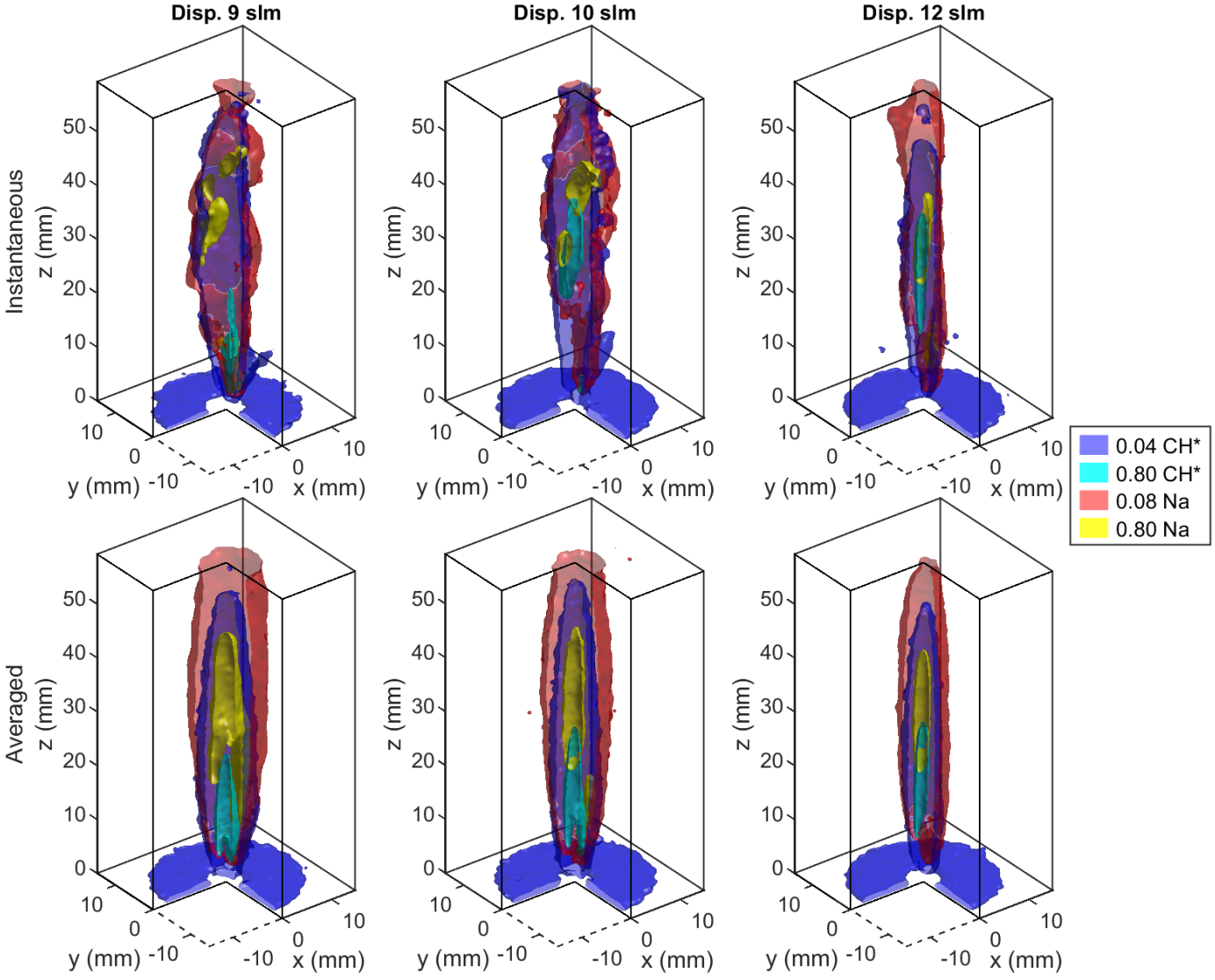

Figure 3. Instantaneous (top row) and time-averaged (bottom row) reconstructed fields of CH* and Na for turbulent spray flames at different flow rates of the dispersion gas (columns).

the hot spray-flame products that are larger and more undulated. The latter characteristics are strengthened by the expansion of the burnt gases, as a result of heat release (Martins et al., 2020). Generally, the maximum intensities of the Na fields occur at further downstream regions compared to those of CH* fields. This is expected, because the Na signal mostly appears downstream the flame front, due to the upward main stream motion and buoyancy effect (Martins et al., 2020). The time-averaged fields show slightly asymmetric flame structures close to the burner exit that evolve towards symmetric structures about the z-axis for downstream positions. The asymmetric flame front morphology at upstream locations translates to an asymmetric temperature-composition field that can ultimately lead to inhomogeneous final synthesized material, as observed in other works (Stodt et al., 2021; Bieber et al., 2021; Tischendorf et al., 2021). The asymmetry seems to be caused by inaccuracies in the inner nozzle geometry and potential minor misalignment; both are critical in this small-sized burner. The asymmetries might also indicate a spatially-inhomogeneous size distribution of atomized droplets, which could impact on the droplet velocity (Martins et al., 2021) broadening the temperature-concentration history experienced by the nanoparticle in FSP. The general shape of the time-averaged spray flames resembles a prolate ellipsoid. This shape is in agreement with that inferred from the high-temperature zones in the time-averaged thermocouple measurements of Gonchikzhapov & Kasper (2020) assuming symmetry about the spray-flame centerline. The time-averaged structures of spray flames are shorter and narrower for greater dispersion gas flow rates. This seems to be the result of a better atomization process, as discussed in the work of Stodt et al. (2019). They showed that the size distribution of atomized droplets in the twin-fluid nozzle, measured by means of a dual phase-Doppler anemometer, shifts towards smaller values when the flow rate of the dispersion gas increases. Since smaller droplets fully evaporate faster, the overall combustion process is accelerated, leading to a more constricted spray flame.

The coexistence of CH* and Na signals can be better visualized in combined color slices using RGB images. Horizontal and vertical slices of instantaneous and time-averaged fields of CH* (blue channel) and Na (red channel) are presented in Fig. 4 for the flow condition SF1 ($10\,\mathrm{slm}$ dispersion gas). Intensities are normalized within each slice. The combined color magenta represents regions where both flame front and hot flame-spray products coexist, overcoming possible ambiguous interpretations from line-of-sight or planar measurements. The instantaneous slices reveal the turbulent characteristic of the flame and the structural detail resolved by the present measurements. The time-averaged intensities of CH* and Na show a dual-peak distribution near the burner exit that develops towards a bell-shaped distribution downstream.

Normalized profiles along the z and x axes of time-averaged reconstructed fields of CH* and Na signal are presented in Fig. 5 for the standard operating condition SF1. The intensity values of the vertical profiles of CH* and Na monotonically increase up to a maximum and then monotonically decrease further downstream. The greatest intensity of CH*, at $z \approx 17\,\mathrm{mm}$, reflects the most intense reaction zone of the spray flame, whereas the greatest intensity of Na emission at $z \approx 37\,\mathrm{mm}$ is linked to a combined effect of high concentrations of spray-flame products with a high-temperature region. The profiles along the x-axis of CH* and Na evolve from asymmetric

distributions close to the nozzle exit towards bell-shaped distributions for downstream positions. The profiles of Na at $z = 10\,\mathrm{mm}$ show a dual-peak distribution due to the liquid spray.

Time-averaged fields of CH* and Na signal are used to quantify features characterizing the spray flames, namely height (location where the intensity along the flame centerline decreases to $10\,\%$ of the maximum value downstream), full width at half maximum (FWHM, width measured between two points along the radial profile where the intensities are half of the maximum value) and tilt angle (angle between flame centerline and the z-axis). The flame centerline is obtained by least-

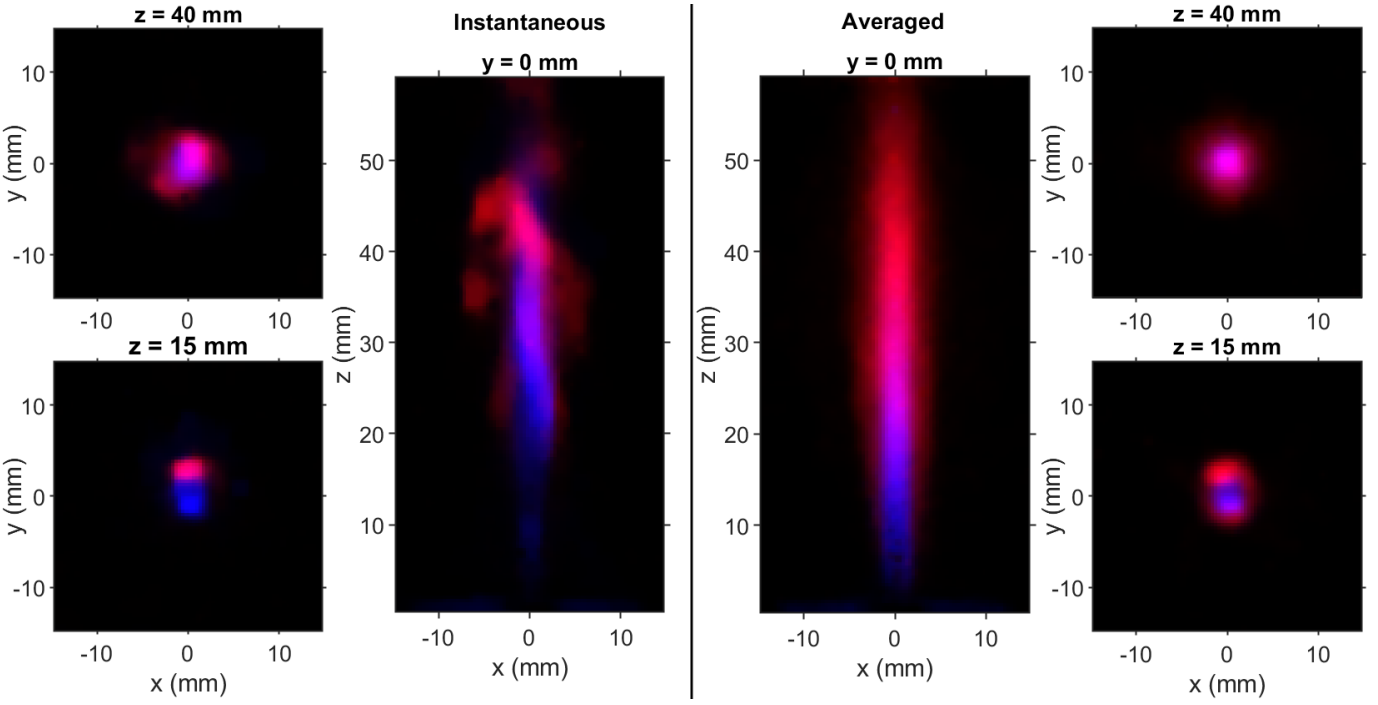

Figure 4. Horizontal and vertical slices from instantaneous (left) and time-averaged (right) reconstructed fields of CH* (blue channel) and Na (red channel) under the standard operating condition SF1.

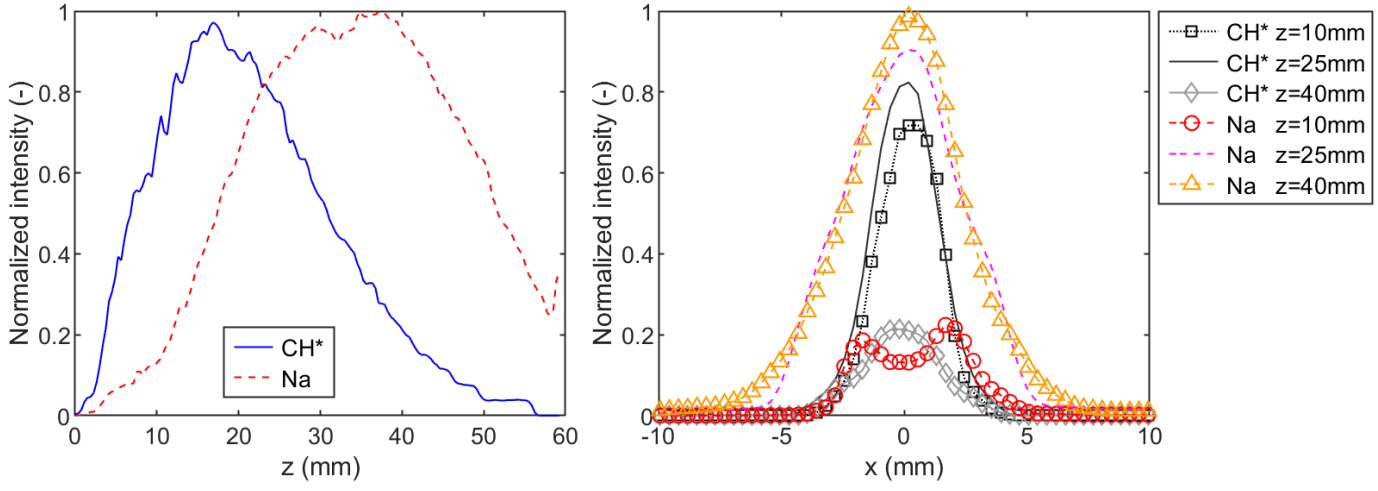

Figure 5. Normalized intensity profiles along z-axis (left) and x-axis (right) for the time-averaged field of CH* and Na under the standard operating condition SF1.

squares fitting a 3D line over the peak intensities in various horizontal slices. The FWHM is calculated at $z = 30\,\mathrm{mm}$ because both measurements show good signal-to-noise levels. The comparison of the features is presented in Fig. 6 for the investigated operating conditions. The spray-flame widths from the averaged CH* fields varies from 3 to $4\,\mathrm{mm}$, and the heights from 43 to $47\,\mathrm{mm}$ according to the operating condition. The widths from averaged Na fields are broader, ranging from 3.5 to $8.5\,\mathrm{mm}$, and the heights are longer, expanding further downstream of the investigated domain. Generally, the flame height and width decreases when increasing dispersion gas. This is probably a consequence of smaller atomized droplets, as discussed previously. The flame tilt angles vary from 0.2 to $0.5°$. The lowest angle of $0.2°$ is observed for $10\,\mathrm{slm}$ dispersion gas, which is expected since the nozzle is aligned based on this operating condition.

Scatter plots from horizontal slices of CH* and Na intensity fields are presented in Fig. 7 to analyze the association between both fields. The CH* and Na intensity fields are normalized by their corresponding maximum intensities. The instantaneous cases plotted in the top row of the figure are the same ones visualized by isosurfaces in Fig. 3. Due to the turbulent characteristic of the spray flames, the scattered plots of instantaneous fields are very different from each other with respect to different time instances (not presented due to space constraints) and operating conditions. Nevertheless, a general trend can be observed. The greatest intensity values of CH* are found at $z < 20\,\mathrm{mm}$ and are associated with middle and low intensity values of Na, while the greatest intensity values of Na are related to middle and low intensity values of CH*. This is expected because the Na signal is detected on the burnt side of the spray flame, whereas the CH* signal is detected at the flame front, as aforementioned. The time-averaged cases plotted in the bottom row of Fig. 7 show a clearer trend. The distributions close to the burner exit ($z < 20\,\mathrm{mm}$) are very spread out characterizing a weak association between CH* and Na for all cases, but evolve towards con-

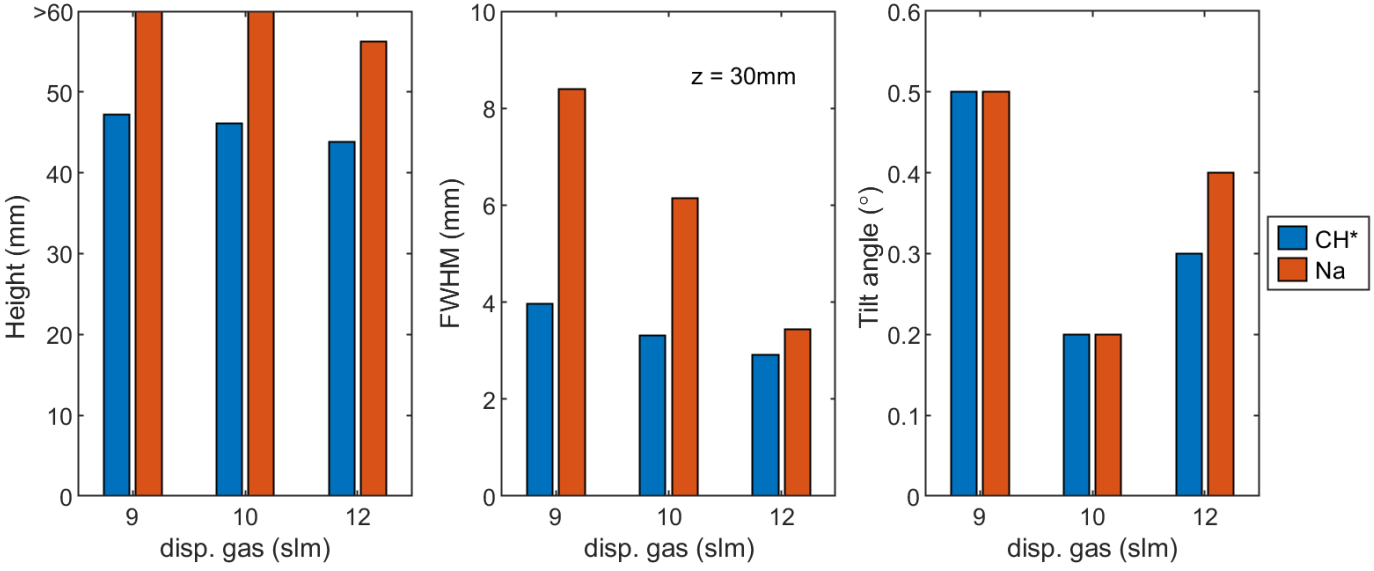

Figure 6. Height, full width half maximum at $z = 30\,\mathrm{mm}$ and tilt angle for the time-averaged field of CH* and Na for different flow rates of the dispersion gas.

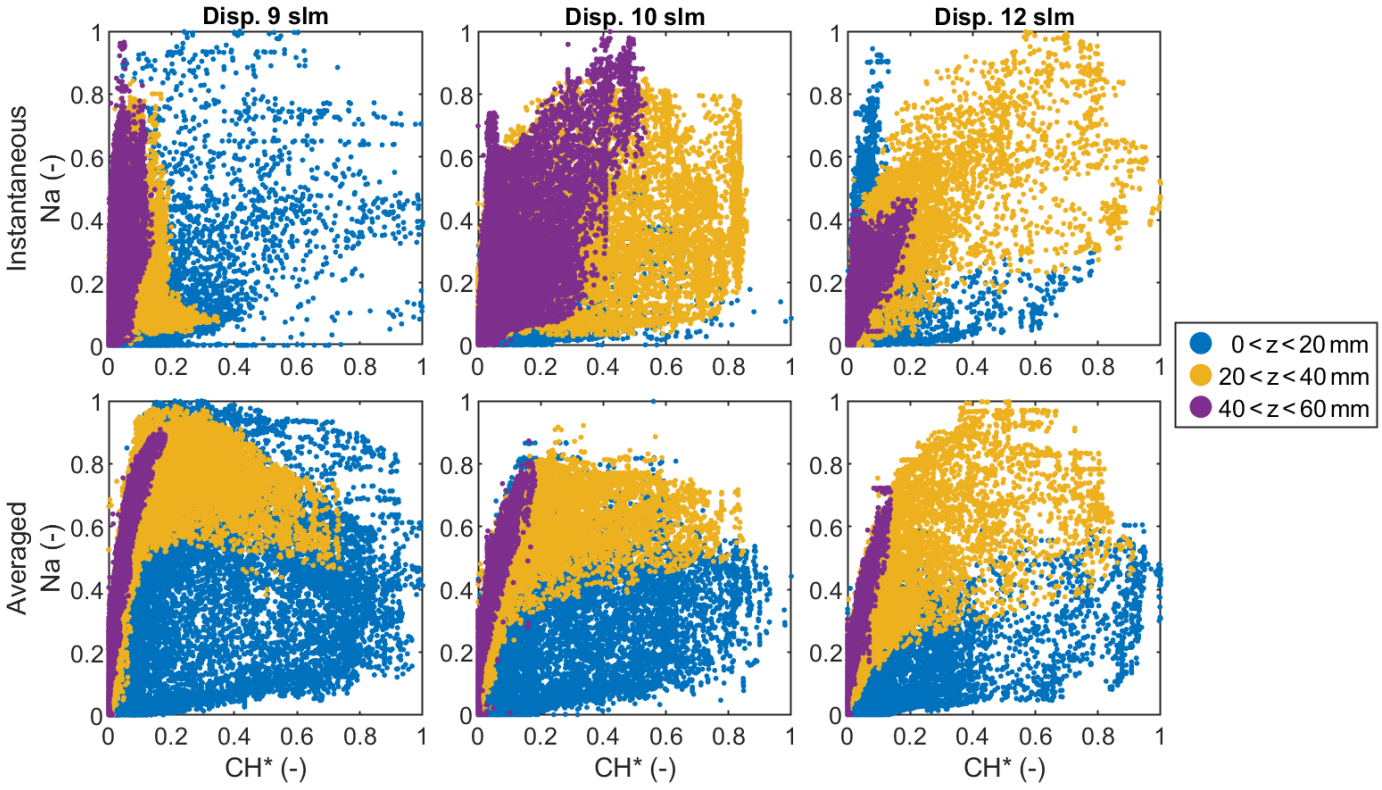

Figure 7. Scatter plots of normalized CH* and Na signals from instantaneous (top row) and time-averaged (bottom row) reconstructions at various height intervals for different flow rates of the dispersion gas (columns).

stricted distributions downstream ($40 < z < 60\,\mathrm{mm}$) describing a positive strong linear association. In the latter region, greater Na signals are linked to lower CH* signals. This is expected due to the upward motion of the hot spray products. The small asymmetries in the spray flames observed previously (e.g., Fig. 3 and Fig. 4) are expected to increase the spread of points in the plots of Fig. 7.

4. Conclusions

Tomographic imaging using multi-simultaneous measurements was applied to investigate turbulent spray flames issued through the SpraySyn burner at three operating conditions. Such spray flames are designed for nanoparticle synthesis in FSP. Instantaneous and time-averaged 3D fields of CH* chemiluminescence (flame front marker) and Na emission from NaCl dissolved in the liquid solution (hot spray-flame products indicator) were reconstructed from concurrent measurements.

The 3D reconstructed fields revealed the flame morphology in detail with regions of mixing and interaction between the flame front and spray stream. The association between CH* and Na were investigated by means of isosurface visualizations, combined slices, profiles and scattered plots. CH* structures were generally more constricted along the flame centerline, while Na structures were much broader and spanned further downstream of the investigated domain. The time-averaged

reconstructions display spray flames always with some level of asymmetry near the burner exit, which might lead to inhomogeneous properties of the final synthesized material in FSP processes. However, the flames develop towards more symmetrical structures with horizontal cross-sections exhibiting bell-shaped distributions of the measured signals at downstream locations. The measured heights and widths of the spray flames decreases with the increase of the flow rate of dispersion gas, which might be caused by the differences in the size distribution of atomized droplets. The flame inclination can be as low as $0.2°$ with careful nozzle alignment.

Aiming more symmetrical spray flames for FSP, we plan to investigate an improved version of the SpraySyn burner equipped with an optimized twin-fluid nozzle (Bieber et al., 2021) in future work by applying TIMes for reconstructing even more concurrent fields.

Acknowledgments

The authors gratefully acknowledge the computing time provided by the Paderborn Center for Parallel Computing (PC^2) and the funding from the German Research Foundation (DFG) within the priority program "Nanoparticle Synthesis in Spray Flames, SpraySyn: Measurement, Simulation, Processes" (SPP1980, project number 447391812).

References

Bieber, M., Al-Khatib, M., Fröde, F., Pitsch, H., Reddemann, M. A., Schmid, H. J., et al. (2021). Influence of angled dispersion gas on coaxial atomization, spray and flame formation in the context of spray-flame synthesis of nanoparticles. *Experiments in Fluids*, *62*(5), 1–13.

Foo, C. T., Unterberger, A., Martins, F. J. W. A., Prenting, M. M., Schulz, C., & Mohri, K. (2022). Investigating spray flames for nanoparticle synthesis via tomographic imaging using multi-simultaneous measurements (TIMes) of emission. *Optics Express*, *30*(9), 15524–15545.

Foo, C. T., Unterberger, A., Menser, J., & Mohri, K. (2021). Tomographic imaging using multi-simultaneous measurements (TIMes) for flame emission reconstructions. *Optics Express*, *29*(1), 244.

Gonchikzhapov, M., & Kasper, T. (2020). Decomposition reactions of $Fe(CO)_5$, $Fe(C_5H_5)_2$, and TTIP as precursors for the spray-flame synthesis of nanoparticles in partial spray evaporation at low temperatures. *Industrial & Engineering Chemistry Research*, *59*(18), 8551–8561.

Martins, F. J. W. A., Kirchmann, J., Kronenburg, A., & Beyrau, F. (2020). Experimental investigation of axisymmetric, turbulent, annular jets discharged through the nozzle of the SPP1980 SpraySyn burner under isothermal and reacting conditions. *Experimental Thermal and Fluid Science*, *114*, 110052.

Martins, F. J. W. A., Kirchmann, J., Kronenburg, A., & Beyrau, F. (2021). Quantification and mitigation of PIV bias errors caused by intermittent particle seeding and particle lag by means of large eddy simulations. *Measurement Science and Technology*, *32*(10), 104006.

Meierhofer, F., & Fritsching, U. (2021). Synthesis of metal oxide nanoparticles in flame sprays: Review on process technology, modeling, and diagnostics. *Energy & Fuels*, *35*(7), 5495–5537.

Mohri, K., Görs, S., Schöler, J., Rittler, A., Dreier, T., Schulz, C., & Kempf, A. (2017). Instantaneous 3D imaging of highly turbulent flames using computed tomography of chemiluminescence. *Applied Optics*, *56*(26), 7385.

Mosburger, M., Sick, V., & Drake, M. C. (2014). Quantitative high-speed imaging of burned gas temperature and equivalence ratio in internal combustion engines using alkali metal fluorescence. *International Journal of Engine Research*, *15*(3), 282–297.

Schneider, F., Suleiman, S., Menser, J., Borukhovich, E., Wlokas, I., Kempf, A., et al. (2019). SpraySyn – A standardized burner configuration for nanoparticle synthesis in spray flames. *Review of Scientific Instruments*, *90*(8).

Schulz, C., Dreier, T., Fikri, M., & Wiggers, H. (2019). Gas-phase synthesis of functional nanomaterials: Challenges to kinetics, diagnostics, and process development. *Proceedings of the Combustion Institute*, *37*(1), 83–108.

Stodt, M. F. B., Kiefer, J., & Fritsching, U. (2019). Ethanol droplet formation, dynamics and combustion mode in the flame of the SpraySyn-nozzle. *Experiments in Fluids*, *60*(8), 1–11.

Stodt, M. F. B., Liu, C., Li, S., Mädler, L., Fritsching, U., & Kiefer, J. (2021). Phase-selective laser-induced breakdown spectroscopy in flame spray pyrolysis for iron oxide nanoparticle synthesis. *Proceedings of the Combustion Institute*, *38*(1), 1711–1718.

Tischendorf, R., Simmler, M., Weinberger, C., Bieber, M., Reddemann, M., Fröde, F., et al. (2021). Examination of the evolution of iron oxide nanoparticles in flame spray pyrolysis by tailored *in situ* particle sampling techniques. *Journal of aerosol science*, *154*, 105722.

Unterberger, A., Kempf, A., & Mohri, K. (2019a). 3D evolutionary reconstruction of scalar fields in the gas-phase. *Energies*, *12*(11), 2075.

Unterberger, A., Menser, J., Kempf, A., & Mohri, K. (2019b). Evolutionary camera pose estimation of a multi-camera setup for computed tomography. In *2019 IEEE International Conference on Image Processing (ICIP)* (pp. 464–468).

Unterberger, A., & Mohri, K. (2022). Evolutionary background-oriented schlieren tomography with self-adaptive parameter heuristics. *Optics Express*, *30*(6), 8592–8614.